

## MIT Open Access Articles

*Spectral, spatial and polarization-selective perfect absorbers with large magnetic response for sensing and thermal emission control*

The MIT Faculty has made this article openly available. **Please share** how this access benefits you. Your story matters.

**Citation:** Tsurimaki, Yoichiro et al. "Spectral, spatial and polarization-selective perfect absorbers with large magnetic response for sensing and thermal emission control." *Optics Express*, 27, 26 (July 2019): A1041-A1059 © 2019 Optical Society of America under the terms of the OSA Open Access Publishing Agreement

**As Published:** <http://dx.doi.org/10.1364/oe.27.0a1041>

**Publisher:** The Optical Society

**Persistent URL:** <https://hdl.handle.net/1721.1/123868>

**Version:** Final published version: final published article, as it appeared in a journal, conference proceedings, or other formally published context

**Terms of Use:** Article is made available in accordance with the publisher's policy and may be subject to US copyright law. Please refer to the publisher's site for terms of use.





# Spectral, spatial and polarization-selective perfect absorbers with large magnetic response for sensing and thermal emission control

YOICHIRO TSURIMAKI, SVETLANA V. BORISKINA, YI HUANG, AND GANG CHEN\*

*Department of Mechanical Engineering, Massachusetts Institute of Technology, Cambridge, MA, 02139, USA*

*\*gchen2@mit.edu*

**Abstract:** Spectral, spatial, and polarization selective perfect absorption of light in periodic metal-dielectric-metal nanoslits, each of which supporting a single electric-field anti-symmetric surface mode, is systematically studied. Our numerical analysis shows complete absorption of  $p$ -polarized light associated with large magnetic field enhancement at wavelengths from the visible to the mid-infrared range and roles played by the geometrical parameters of the structure. This understanding is then applied to the design of the structure with multiple nanoslits in a period that exhibits complete absorption at multiple wavelengths. Semi-analytical expression of the zeroth mode reflectance is derived, which shows a good agreement with numerical simulations and yields clear insight into the underlying physics of light-matter interactions in the structure.

© 2019 Optical Society of America under the terms of the [OSA Open Access Publishing Agreement](#)

## 1. Introduction

Strong absorption of light by nanostructured materials at desired wavelengths and with a specific angular distribution is of great interest for photonics and optoelectronics technologies as it directly contributes to high sensitivity of optical sensors [1,2], high-efficiency photovoltaic devices and photodetectors [3–5], and provides mechanisms for spectral shaping of thermal emission from terrestrial heat sources [6–10]. To achieve strong light absorption, nanostructured materials are often designed to support either surface plasmon polaritons (SPPs) or surface phonon polaritons (SPhPs), which enable efficient guiding and confinement of light at resonant frequencies in the visible to near-infrared, and in the mid-infrared spectral bands, respectively. The strong interaction between light and matter via the excitation of SPPs and SPhPs underlies the physics of the extraordinary optical transmission [11,12] and resonant absorption [13–22]. It also yields a wide range of potential applications, including highly-sensitive optical sensors [1,23–25], efficient photovoltaic devices [4,26,27], high-resolution and high-sensitivity spectroscopy [23,24,28,29], as well as partially-coherent efficient thermal emitters [7,30–33]. In order to couple the propagating light waves to the SPPs or SPhPs on planar surfaces, external couplers such as prisms or nanostructured materials are necessary since the surface waves cannot be directly excited due to their large lateral momenta. In the context of optical absorption via SPPs excitation, one of the most-studied nanostructures is a metallic grating. Since the discovery of the Wood anomaly [34], the complete absorption of light incident upon grating structures has been extensively studied, both theoretically and experimentally [19,20,35]. In the metallic grating structures, the incident light is coupled to propagating SPPs supported at the metal-air interface via the momentum gain due to the periodicity of the gratings.

When the light is coupled to the propagating SPPs, the resonant frequency is determined by the intrinsic plasma frequency of the material, which for metals typically lies in the UV to

the visible frequency range. The resonant absorption at longer wavelengths is achieved by either coupling to propagating SPPs supported by materials with lower bulk plasma frequencies [36] such as semiconductors or by coupling to localized SPPs modes, whose resonant frequency is tunable by nanostructure size and geometry [37,38]. Additional tuning of the SPPs resonant frequency can be achieved in retardation-based plasmonic structures. Retardation-based gratings, unlike conventional quasi-static ones, incorporate a thin dielectric layer, which is sandwiched between the metallic gratings and the metallic substrate. The two terminations of each metallic grating form a truncated metal-dielectric-metal waveguide, and the complete absorption is attained by coupling the light into the localized SPPs supported at the metal-dielectric interfaces underneath metallic gratings [39–41].

Another type of metal-dielectric nanostructure that exhibits the resonant absorption via the excitation of localized SPPs is a metallic nanoslit filled with dielectrics [42,43]. Unlike the grating structures mentioned above, where the localized SPPs are excited parallel to the surface, the nanoslit supports the localized SPPs that propagate in the depth direction of nanoslits, i.e., perpendicular to the surface. This enables two-dimensional spatial localization of energy in the absorber as well as spatial and spectral splitting of absorbed light. Previously [42,43], a single metal-dielectric-metal nanoslit structure was studied to demonstrate the large enhancement of absorption and to investigate effects of geometrical parameters of the single nanoslit on the enhancement of absorption at a given wavelength of incident light. Here, we examine periodic nanoslit structures under the incidence of broadband light in order to achieve complete absorption at multiple wavelengths, which is useful for optical sensors and light sorting. We are also interested in evaluating the effects of geometrical parameters on the spectral and directional reflectance or emittance of the structure for potential thermal applications. In this work, we systematically investigate optical absorption by a periodic nanoslit structure shown in Fig. 1, in which each nanoslit supports only an electric-field anti-symmetric surface mode propagating in the depth direction of the slits, i.e.,  $y$ -direction. This electric-field anti-symmetric surface mode is also known as the long-range SPPs excited in a thin metal film, which is a coupled mode of the two SPPs at the two interfaces between the metal film and the surroundings [44]. The difference from the long-range SPPs excited in a thin metal film is that the propagation direction of the anti-symmetric surface mode is perpendicular to the surface of the structure, thereby no optical couplers are necessary to couple the energy of propagating waves into this mode. By properly designing the structure, the perfect resonant absorption of  $p$ -polarized incident light is possible at three widely different wavelengths. Our focus in this paper is to engineer the complete absorption of light in a periodic nanoslit structure from the visible to the infrared range and to describe the detailed design procedure to achieve it. In our structure, the perfect absorption is not due to the surface-plasmon mode excited at the metal-air interface, propagating in the  $x$ -direction as often is the mechanism of complete absorption in metallic gratings. Moreover, we reveal the roles played by different geometrical parameters in attaining complete absorption and give physical insight by deriving the semi-analytical expression of reflectance, which can also serve for fast implementation of structure design.

The structure in Fig. 1 enables complete absorption of  $p$ -polarized light at desired wavelengths and angles of incidence and is especially attractive for the following reasons. First, nanoslits support the electric-field anti-symmetric surface mode, which has neither lower nor upper cutoff wavelength [45,46]. Thus, the resonant absorption of incident light at a wide range of wavelengths from the visible to the infrared is in principle possible. Furthermore, by scaling the geometry of an individual nanoslit, it can exhibit a large absorption cross-section, making possible the complete absorption of light in the structure with the period  $d$  comparable to the incident wavelength  $\lambda$ . Second, because the directions of the structural periodicity ( $x$ -direction) and the wave propagation in the nanoslits ( $y$ -direction) are decoupled, the scaling of the nanoslit depth  $h$  – which determines its resonant frequency – is weakly affected by the period of the

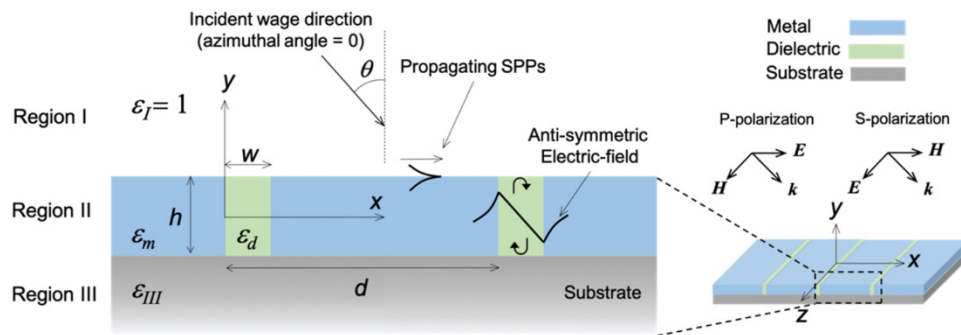


Fig. 1. Schematic of periodic nanoslit structure (on the right) and its cross-sectional view on the  $x$ - $y$  plane (on the left). Nanoslits formed by a metallic material with dielectric function  $\epsilon_m$  are filled with a dielectric with  $\epsilon_d$ . The substrate is a material with dielectric function  $\epsilon_{III}$  and is in general different from the materials in the region II. The incident light is assumed to be on the  $x$ - $y$  plane, i.e., the azimuthal angle is zero. Complete absorption is due to coupling to the electric-field anti-symmetric surface mode supported in nanoslits (typical field distribution of the  $y$ -component of the electric field is depicted), but not due to propagating SPPs at the surface.

structure  $d$ . This allows to keep the metallic fraction of the surface high and makes possible to design the system such that it attains the complete absorption at the resonant wavelength while maintaining high reflectance everywhere else. Moreover, by locating multiple nanoslits in a period so that each nanoslit supports the resonant modes at different wavelengths, the structure functions as a multi-band perfect absorber, which can be used for light sorting.

Previously [47], a bi-grating structure was proposed to achieve spectrally-selective absorption of incident light at two different wavelengths in each of the two slits. By using  $TM_1$  guided mode and far-field coupling of the scattered fields from the two slits, the large absorption and thus the near-unity light sorting efficiency were reported. In our structure, we use an electric-field anti-symmetric surface mode to achieve perfect absorption at multiple wavelengths. The perfect absorption at each wavelength is due to a large absorption cross-section of each nanoslit, not due to either the near-field or far-field coupling of the two slits. We will show that the perfect absorption of light at widely-separated wavelengths is possible by using nanoslits of different heights, as well as different widths. Finally, the angular dependence of the structure absorptance can be tailored by exciting the propagating SPPs in the  $x$ -direction at the top metal-air interface by changing the periodicity without affecting much the resonant frequency of a nanoslit. As a result, a highly absorbing structure for an incident light from a given angle of incidence can turn into a highly reflective structure for the light at another angle of incidence.

Unlike previously studied perfect metamaterial absorbers [21,22], this periodic nanoslit structure is not amenable to modeling as an effective medium and requires precise electromagnetic modeling that accounts for the boundary conditions on each nanoslit. Development of a simple semi-analytical approach to model such an absorber is therefore highly desirable in order to reduce the computational effort in optimizing the structure design for various applications and to gain physical insight into the light confinement and absorption process. An efficient semi-analytical forward-modeling method will also form the basis for machine-learning inverse-design approaches to optimize and customize multi-band absorbers and thermal emitters in the future.

The paper is organized as follows. First, we outline a design procedure to create a periodic nanoslit structure that supports only an anti-symmetric surface mode but no oscillating mode. Then, following this design procedure, the perfect absorption of light at three widely different wavelengths from the visible to mid-infrared is numerically demonstrated. The different roles played by various geometrical parameters of the structure are discussed. Our analysis reveals

that the SPPs modes at the top metal-air interface of the structure do not contribute to the absorption, making complete absorption possible regardless of the structure periodicity. We then provide the semi-analytical expression of the zeroth mode reflectance of the periodic nanoslit structure. The semi-analytical expression not only allows to reveal the physical mechanisms underlying the perfect absorption but also simplifies and speeds up the design process. We discuss applications of the periodic nanoslit structure for optical phase-sensing, directional thermal emission, and multi-band perfect absorption. Finally, we also study the effects of fillets at the edges of the nanoslits on absorptance and demonstrate the perfect absorption even in the presence of structural degradation during fabrication processes.

## 2. Design strategy to model and optimize the perfect absorber

Figure 1 shows a schematic of the periodic nanoslit structure on which the light is incident at an angle  $\theta$  from the air. We assume that the nanoslits are infinitely long in the  $z$ -direction, and the wavevector of the incident light is on the  $x$ - $y$  plane, i.e., the azimuthal angle of the incident light is zero. For the  $p$ -polarized incident light, the magnetic field points in the  $z$ -direction. We separate the structure in three regions in the  $y$ -direction as shown in Fig. 1. The region I ( $y > h/2$ ) is the air, i.e., the dielectric function is  $\epsilon_I = 1$ . The region II ( $-h/2 \leq y \leq h/2$ ) consists of a material with dielectric function  $\epsilon_m$  and nanoslits of width  $w$  and depth  $h$  filled by a material with dielectric function  $\epsilon_d$ . Our interest especially lies in the case where the material filling the nanoslits is a dielectric and the material that forms nanoslits is a metal, i.e.,  $\text{Re}[\epsilon_d] > 0$  and  $\text{Re}[\epsilon_m] < 0$ . Thus, we hereafter refer to the materials with  $\epsilon_d$  and  $\epsilon_m$  in the region II in Fig. 1 as the dielectric and the metal, respectively. The nanoslits are located on top of an optically thick substrate with dielectric constant  $\epsilon_{III}$ . In this work, we only consider the case where the substrate is the same material as the metal in the region II, i.e.,  $\epsilon_m = \epsilon_{III}$ . However, the semi-analytical expression we derive in the later section of the paper is valid for general cases where the substrate is different from the materials in the region II. All the materials are assumed non-magnetic and their optical properties do not show spatial dependence and dispersion. In this work, we generally consider that the nanoslit width  $w$  is sufficiently small compared to the wavelength of the incident light in the free space. This condition is to ensure that no guided mode is supported in the nanoslit, which we will discuss in more detail in the next section. As we will show later in Fig. 2(b), the relation between the width and the incident wavelength needs to be roughly  $w/\lambda \leq 1/7$  in the case of silicon and silver.

### 2.1. Modal structure of the metal-dielectric-metal nanoslit

It is known that an infinitely-long slab waveguide in which claddings have a negative dielectric constant – a metal-dielectric-metal (MDM) waveguide – supports both oscillating modes and SPP modes [46] as shown in Fig. 2 (a). We only consider the symmetric waveguide where two metallic claddings are comprised of the same material. Oscillating modes in the infinitely-long MDM waveguide have propagation constants in the range  $0 < \beta < \sqrt{\epsilon_d} k_0$ , where  $k_0 = \omega/c_0$  is the wavenumber in a vacuum given by the frequency  $\omega$  and the speed of light in vacuum  $c_0$ . The propagation constant  $\beta$  is the wavenumber of the mode in the  $y$ -direction in Fig. 2 (a). The oscillating modes in a MDM waveguide are analogous to modes guided by total internal reflection in a dielectric slab waveguide, i.e., cladding has a positive dielectric constant, but have different mode cutoff values. Also, the range of propagation constant is different from that of a dielectric slab:  $\sqrt{|\epsilon_m|} k_0 < \beta < \sqrt{\epsilon_d} k_0$  and this fact allows the externally incident light to couple more efficiently to the waveguide.

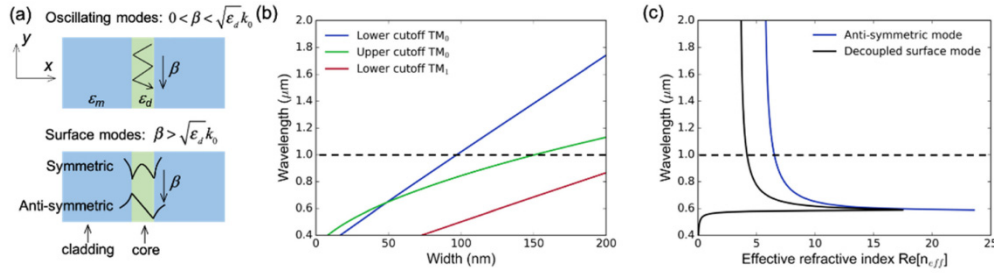


Fig. 2. (a): Schematic of oscillating modes and surface modes propagating in the  $y$ -direction in an infinitely-long MDM waveguide. In oscillating modes, wave propagation is analogous to a mode guided by total internal reflection in a dielectric slab waveguide. For surface modes, typical  $y$ -component field distributions of the electric field for symmetric and anti-symmetric surface modes are shown. Dispersion relations of (b) lower and upper cutoff wavelengths of  $\text{TM}_0$  and  $\text{TM}_1$  modes, and (c) the anti-symmetric surface polariton mode in the nanoslits and the surface polariton mode supported by a single Si-Ag planar interface.

The dispersion relations of the TE and TM oscillating modes are given as:

$$\begin{aligned}
 k_x^d w &= 2 \arctan \left( \frac{k_x^m}{k_x^d} \right) + l\pi \quad \text{TE}_l \text{ mode} \\
 k_x^d w &= -2 \arctan \left( \frac{\epsilon_m k_x^d}{\epsilon_d k_x^m} \right) + l\pi \quad \text{TM}_l \text{ mode}
 \end{aligned} \tag{1}$$

where  $k_x^d = \sqrt{\epsilon_d k_0^2 - \beta^2}$  and  $k_x^m = \sqrt{\beta^2 - \epsilon_m k_0^2}$  are the wavevectors in the  $x$ -direction in the core and the claddings, respectively, and  $l = 0, 1, 2, \dots$ . We used the superscripts  $d$  and  $m$  to indicate that the core and the claddings are dielectric and metallic materials, respectively.  $\text{TE}_l$  mode has the same lower cutoff as  $\text{TM}_l$  mode while they do not have an upper cutoff except the lowest modes  $\text{TM}_0$  that has an upper cutoff. Hence, by creating a waveguide with a sufficiently small width so that it does not support  $\text{TM}_0$  mode, the waveguide does not support  $\text{TE}_0$  mode either. Usually, higher modes are not supported either when the lower-numbered modes are not supported. As a result, we can create a waveguide that will not support oscillating modes of any polarization by making the width smaller than the lower cutoffs of the oscillating modes. In addition to the oscillating modes, the surface polariton modes can be excited in the MDM waveguide under the  $p$ -polarized light illumination, as the core and cladding have dielectric constants of opposite sign. Surface modes are different from oscillating modes in that they have larger propagation constants  $\beta > \sqrt{\epsilon_d} k_0$ , and their field intensity exponentially decays away from the interface into both of the core and cladding. The surface polariton modes in infinitely-long symmetric waveguides, i.e., when two cladding materials are identical, can form two coupled modes as a result of interference of the modes at the two core-cladding interfaces in a waveguide. The electric field of such coupled mode is either symmetric or anti-symmetric about the center of the waveguide. Typical distributions of the  $y$ -component of the electric field of the symmetric and anti-symmetric surface modes are shown in Fig. 2 (a). It has been shown that the anti-symmetric surface mode has neither lower nor upper cutoff wavelengths for  $\epsilon_d < |\epsilon_m|$  [48], which means that for a given geometry of the waveguide, the anti-symmetric surface mode with any frequency is physically allowed to exist. This condition  $\epsilon_d < |\epsilon_m|$  is satisfied for most combinations of dielectric and metal at wavelengths longer than the visible spectrum. As mentioned at the beginning of the section, the signs of the dielectric functions of the dielectric and metal must be opposite. In the mid-infrared wavelength range, some polar dielectrics support bulk polaritons and their dielectric

functions become negative. In this range, the above condition is not satisfied, and the anti-symmetric surface mode cannot be supported. Furthermore, the real part of the dielectric function can have a large positive value below the frequency of the transverse optical phonon, and a near zero value at above the frequency of the longitudinal optical phonon. In the former case, the condition  $\varepsilon_d < |\varepsilon_m|$  may not be supported depending on the choice of materials. In the latter case, the lower cutoff of the  $TM_0$  mode scales as  $w_{\min} \sim \lambda / 2 / \sqrt{\varepsilon_d}$  and the nanoslits do not need to be sufficiently small compared to the wavelength of the incident light in the free space in order to suppress all the guided modes.

The symmetric surface mode has a lower cutoff but no upper cutoff wavelength, i.e., there exists the maximum wavelength of the mode above which the symmetric surface mode cannot be supported for a given geometry of waveguide. However, the symmetric mode cannot be excited by the externally incident  $p$ -polarized light because the electric field of the  $p$ -polarized incident light is anti-symmetric about the center of the waveguide. Therefore, by reducing the waveguide width such that it is less than the cutoff wavelengths of the oscillating modes, the infinitely long MDM waveguide can be designed to support only the anti-symmetric surface mode and no oscillating modes upon the externally incident  $p$ -polarized light. Up to this point, we discussed that we can create an infinitely-long MDM waveguide that only supports the anti-symmetric surface mode. Although nanoslits in Fig. 1 are different from an infinitely-long MDM waveguide in that they are truncated and periodic, the same argument about the MDM waveguide can be valid. In our structure, the dielectric and the metal in the region II correspond to the core and the cladding of a MDM waveguide, respectively, in the discussion above. First, the dispersion relation of the infinitely-long MDM waveguide describes the dispersion relation in the nanoslits reasonably well unless the nanoslit is too shallow. Second, the anti-symmetric surface mode is spatially confined in the lateral direction ( $x$ -direction in Fig. 1), which makes each nanoslit in the periodic structure independent of each other. Since the nanoslits are regarded as truncated MDM waveguides, the surface mode in nanoslits experiences multi-reflection at the two interfaces  $y = \pm h / 2$ , and only constructively-interfered waves exist as standing waves. Therefore, the externally incident light will be strongly coupled to the anti-symmetric surface mode in nanoslits only when the frequencies match those of the standing waves in the nanoslits.

## 2.2. Design of the single-mode MDM slab waveguide

Here, we explain a design procedure of a MDM nanoslit supporting the anti-symmetric surface polariton mode. Figure 2 (b) shows the lower and upper cutoff wavelengths of  $TM_0$  mode and the lower cutoff wavelength of  $TM_1$  mode for different nanoslit thickness  $w$ . The cutoffs are calculated from Eq. (1) by taking the limit  $\beta \rightarrow 0$  and  $\beta \rightarrow \sqrt{\varepsilon_d} k_0$  for lower and upper cutoffs, respectively. Note that the mode index can be different depending on the definition. In fact, the  $TM_0$  mode in our definition corresponds to  $TM_1$  mode in another literature [49]. For the dielectric and the metallic materials, we assumed silicon and silver with optical properties taken from Palik [50] and Yang et al. [51], respectively, i.e.,  $\varepsilon_d = \varepsilon_{Si}$ , and  $\varepsilon_m = \varepsilon_{Ag} = \varepsilon_{Ag}$ . For silicon, we take dielectric constants at the three wavelengths at which the structures are designed to achieve the complete absorption and do not consider the frequency dispersion. In Fig. 2, we used  $\varepsilon_{Si} = 12.75 + i0.002$  which is the dielectric constant of silicon at  $\lambda = 1\mu\text{m}$ . As shown in Fig. 2 (b), once the width of the nanoslit  $w$  becomes smaller than 90nm, no oscillating mode is supported at  $\lambda = 1\mu\text{m}$ . Also, it can be seen that the higher and lower cutoff wavelengths of  $TM_0$  mode are inverted below the waveguide width around 50nm. This inversion is previously proposed as a way to scale the size of a MIM waveguide down to nanoscale [49]. Figure 2 (c) shows the dispersion relation of the anti-symmetric surface mode for the same materials and for the nanoslit width  $w = 30\text{nm}$ . The dispersion relation for the anti-symmetric surface mode is given as [52]:

$$1 + \frac{\epsilon_m k_x^d}{\epsilon_d k_x^m} \tan h \left( -i \frac{k_x^d w}{2} \right) = 0 \quad (2)$$

where  $k_x^d = \sqrt{\epsilon_d k_0^2 - \beta^2}$  and  $k_x^m = \sqrt{\epsilon_m k_0^2 - \beta^2}$  are the wavevectors in the  $x$ -direction in the dielectric and the metal in the region II, respectively. The dispersion relation is solved for the complex propagation constant  $\beta$  of the anti-symmetric surface mode using the Nelder-Mead simplex method [53]. In Fig. 2 (c), the dispersion relation of the surface polariton wave at a single interface between silicon and silver is also shown for comparison. Although it is not shown in Fig. 2 (c), the dispersion of the anti-symmetric surface mode exists even at longer wavelengths than  $2\mu\text{m}$ , as there is no lower cutoff. The upper cutoff of the dispersion exists at around  $\lambda = 585\text{nm}$  below which the condition  $\epsilon_d < |\epsilon_m|$  is not satisfied. Thus, the anti-symmetric surface mode is supported at  $\lambda = 1\mu\text{m}$  with the effective refractive index of around  $n_{\text{eff}} = 6.5$ . Therefore, the nanoslit that only supports the anti-symmetric surface mode at  $\lambda = 1\mu\text{m}$  can be designed by using materials such as silicon and silver once the width of the nanoslit  $w$  is smaller than  $90\text{nm}$ . As the anti-symmetric surface mode does not have a cutoff wavelength, one can vary the width of the nanoslit  $w$  as long as it is less than  $90\text{nm}$  so that the complete absorption of light is achieved. We will show below that the same design procedure can be applied to design nanoslits that support only the anti-symmetric surface mode at longer wavelengths.

### 2.3. Numerical optimization of the MDM nanoslits perfect absorber

Guided by the above design rules, we simulated and optimized the periodic nanoslit structure by using the frequency domain electromagnetic wave solver based on the finite element method. The simulations were performed with the commercial software package COMSOL, using periodic boundary conditions on the two lateral sides of the periodic nanoslit structure, and perfect conductor boundary condition at the bottom of the optically thick substrate. Figure 3 shows spectral reflectance of the three designs of the structure for the  $p$ -polarized incident light at normal incidence. The materials for the dielectric and the metal in the region II and for the substrate are the same for the three structures, i.e. silicon, silver, and silver, respectively. For the dielectric constants of silicon, we take those at the wavelengths at which the complete absorption is designed to happen:  $\epsilon_{\text{Si}} = 12.75 + i0.002$ ,  $\epsilon_{\text{Si}} = 11.79$ , and  $\epsilon_{\text{Si}} = 11.66 + i0.0004$  at  $\lambda = 1\mu\text{m}$ ,  $2.8\mu\text{m}$ , and  $10\mu\text{m}$ , respectively. The structures, which differ only by their geometrical parameters as shown in Fig. 3, show the complete resonant absorption of the  $p$ -polarized incident light at three resonant wavelengths, which lie in the visible ( $\lambda = 1035\text{nm}$ ), near-infrared ( $\lambda = 2.79\mu\text{m}$ ) and mid-infrared ( $\lambda = 9.7\mu\text{m}$ ) parts of the spectrum, respectively. Since the nanoslit width  $w$  of these three structures are small enough to eliminate the existence of oscillating modes at the resonant wavelengths, and – as we will discuss later – the SPPs are not excited, the complete absorption is due to the coupling to the anti-symmetric surface mode. Note that the period of the structures for Fig. 3 (b) and (c) is more than 10 times greater than the nanoslit width. The complete absorption of light even in these sparse nanoslit structures is due to the strong field confinement of the anti-symmetric surface mode and its strong coupling to the incoming free-space radiation. As the structure only supports the single mode, the reflectance is very high for wavelengths longer than the resonant absorption peak. For shorter wavelengths, higher-order surface modes, as well as oscillating modes, can be supported as explained later. In the periodic nanoslit structure, the nanoslit width, depth, and period play

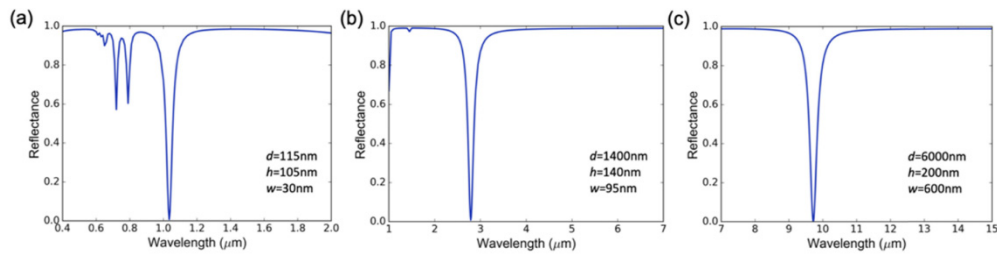


Fig. 3. Spectral reflectance of the periodic nanoslit structure for  $p$ -polarized normally incident light ( $\theta = 0$ ). The dielectric and the metal in the region II and the substrate are silicon, silver, and silver, respectively. The geometrical parameters of the three structures are also shown. For the dielectric constants of silicon, we use:  $\epsilon_{Si} = 12.75 + i0.002$ ,  $\epsilon_{Si} = 11.79$ , and  $\epsilon_{Si} = 11.66 + i0.0004$  for (a), (b), and (c), respectively, and frequency dispersion of silicon is not considered.

different roles in attaining the complete absorption of light. Our analysis below reveals that the choice of the nanoslit depth mainly determines the resonant wavelengths of the structure, while the nanoslit width and the period of the structure can be further tuned to achieve perfect resonant absorption.

When the surface mode is excited by the incident light, it propagates in the nanoslit in the  $y$ -direction in Fig. 1 and experiences multiple reflections between the two interfaces at  $y = \pm h/2$ . As a result, a Fabry-Perot resonant standing wave is formed. Therefore, the resonant wavelength is determined by the Fabry-Perot resonance condition:  $2\text{Re}[\beta]h + \phi = \pi n$ , where  $\beta$  is the propagation constant of the surface mode,  $\phi$  is the phase accumulated upon reflection and  $n$  is the order of the resonance. In the designs in Fig. 3, the lowest order of the Fabry-Perot resonance is used to optimize the structures for complete absorption. This is the reason why the reflectance for longer wavelength than the resonant wavelength is high, while for shorter wavelengths we may expect other absorption peaks due to higher order resonances excitation.

In order to achieve complete absorption, the incident light needs to critically couple to the anti-symmetric surface mode. This is primarily achieved by varying the nanoslit width, which changes the coupling strength of the surface waves at the two interfaces. Remember that the width  $w$  must be varied in the range where no oscillating mode is supported. This results in the variation of the surface mode dissipation, i.e.  $\text{Im}[\beta]$ , as well as the dispersion characteristics of  $\text{Re}[\beta]$ , thus shifting the resonant frequency. By varying the width as well as the depth of the nanoslit, one can maximize the coupling of the incident light into the structure, i.e., the absorption cross-section  $\sigma = Q_{abs} / I_{inc}$ , where  $Q_{abs}$  and  $I_{inc}$  are the power absorbed by being guided in the structure through the nanoslit and the incident flux, respectively. Note that the cross-section  $\sigma$  [m] and the absorbed power  $Q_{abs}$  [W/m] are given per unit length of the structure in the  $z$ -direction as we consider the two-dimensional problem as shown in Fig. 1. In order to achieve complete absorption in the periodic nanoslit structure, the absorption cross-section of each nanoslit aperture needs to be equal to or larger than the period of the structure  $\sigma \geq d$ . The complete absorption of light even in cases where the structure period is more than 10 times greater than the nanoslit width (see Fig. 3) clearly shows that the surface mode can efficiently guide and confine the light in nanoscale volumes.

Figures 4 (a) and (b) show the effects of the period of the structure and nanoslit width on the spectral reflectance of the structure, respectively. The geometrical parameters are varied from those of the structure in Fig. 3 (b). The variation in the period of the structure (Fig. 4 (a)) causes a slight shift in the resonant peak positions compared to the amount of change of the period. Numerical simulation showed that the shift of peak position from the resonant condition of the structure in Fig. 3 (b) ( $d = 1400\text{nm}$ ) is linear and is estimated to be  $\Delta\lambda / \Delta d \sim 4.8 \times 10^{-2}$ . Thus, the reduction of the period by 100nm only shifts the resonant peak

by 5nm. We calculated rigorously the effective refractive index of the surface mode supported in the periodic nanoslit structure by the commercial software Lumerical which solves the electromagnetic fields based on the finite-difference time-domain (FDTD) technique. As a result, we confirmed that the effective refractive index does not change by the variation of the period, which indicates that each nanoslit acts as the independent selective absorber, and the variation of the propagation constant due to the interference between the neighboring nanoslits can be ignored. However, the linewidth  $\Delta\lambda$  of the reflectance broadens as the structure period decreases from  $\Delta\lambda \sim 100\text{nm}$  at  $d = 2000\text{nm}$  to  $\Delta\lambda \sim 200\text{nm}$  at  $d = 700\text{nm}$ , which indicates the contribution from other absorbing channels. However, the variation of the period has little effect on the absorptance; for all the greatly varying period values in Fig. 4 (a), the resonant absorptance of the structure remains greater than 0.8.

Figure 4 (b) illustrates the influence of the nanoslit width on the spectral reflectance of the structure. It shows that the change in the nanoslit width causes the resonant peak shift of almost the same amount; the change of the width is more sensitive to resonant peak position than the change in period. The small width limit of the dispersion relation Eq. (2) gives the relation between the width and the propagation constant as  $\beta w \approx -2\epsilon_d / \epsilon_m$  and the right-hand side of the equation is constant in the long wavelength limit, thereby the reduction of the width increases the propagation constant  $\beta$ . The Fabry-Perot condition for the same mode  $2 \text{Re}[\beta]h + \phi = \pi n$  is still satisfied for an increased propagation constant  $\beta$  due to the decrease of phase pickup  $\phi$  upon reflection [54]. Moreover, the solutions of Eq. (2) as well as the resonant wavelengths show that the overall increase of the propagation constant is achieved by the increase of both the effective refractive index and the resonant wavelength. It also can be seen that the absorptance remains larger than 0.9 for the width variation of around 20nm from the complete absorption condition. This offers flexibility in the structure design and fabrication, making it robust against manufacturing imperfections.

In practice, three geometrical parameters need to be tuned to design a structure that attains the complete absorption of light. Therefore, the design of the structure requires an iterative procedure, which may be time-consuming when fully numerical modeling techniques are used. This motivated us to derive a semi-analytical expression for the reflectance, which is described in the following section.

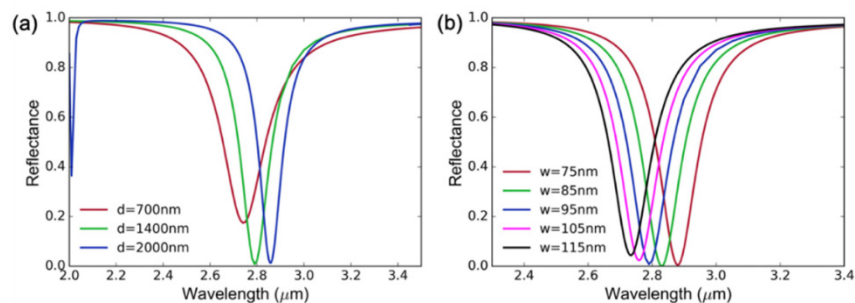


Fig. 4. Effects of period  $d$  and waveguide width  $w$  on the spectral reflectance for  $p$ -polarized normally incident light. The geometrical parameters are varied from the structure in Fig. 3 (b):  $d = 1400\text{nm}$ ,  $h = 140\text{nm}$ , and  $w = 95\text{nm}$ .

### 3. Semi-analytical model of the periodic nanoslit perfect absorber

To verify the hypothesis that the excitation of the anti-symmetric surface mode inside the nanoslits is fully responsible for the perfect absorption and to rule out the absorption by SPPs at the absorber-air horizontal interface, we derive an explicit semi-analytical expression of the zeroth mode reflectance from the designed periodic nanoslit structure. Practically, the semi-analytical expression of the reflectance of the structure makes the design procedure

computationally more efficient. Our semi-analytical model is derived based on prior work by Botten et al. [55–57], which focused on the design of electromagnetics gratings. Other existing semi-analytical models include those based on the modal expansion of fields [35,55–59], the Fabry-Perot cavity models [42], and the temporal-coupled mode theory [43]. However, these models have been developed to study the extraordinary transmission through or reflection from gratings with negligible material losses inside the nanoslit, making them less useful for our analysis. The Fabry-Perot cavity model [42] is proposed to study absorption and gives a simple expression of absorption around single subwavelength nanoslit based on Fresnel reflection coefficients. The Fresnel reflection coefficients can be fitting parameters or derived from the boundary conditions. The temporal coupled mode theory [43] requires the determination of decay rates of each absorption channel for which numerical simulations are usually done. The semi-analytical model introduced here gives a simple expression of absorbance that only requires optical properties and geometrical parameters as inputs and takes the periodicity of the structure into account.

We assume that the  $p$ -polarized light (with the magnetic field in the  $z$ -direction) is incident on the structure at an angle  $\theta$  as shown in Fig. 1. In this case, the magnetic field has only the  $z$ -component ( $H_x = H_y = 0$ ), and all the other field components can be written as functions of  $H_z$ . When the nanoslit width  $w$  is much smaller than the incident wavelength so that no oscillating modes with propagation constants satisfying the condition  $0 < \beta < \sqrt{\epsilon_d} k_0$  are supported, the electromagnetic field in the region II of Fig. 1 is described only by that of the anti-symmetric surface mode. Under this condition, the magnetic fields in the three regions of the structure can be written down as:

$$H_z^I(x, y) = e^{i(k_{0,x}^I x - k_{0,y}^I (y-h/2))} + \sum_{p=-\infty}^{\infty} r_p u_p^I(x) e^{ik_{p,y}^I (y-h/2)} \quad y \geq h/2 \quad (3)$$

$$H_z^{II}(x, y) = (a \sin(\beta y) + b \cos(\beta y)) u^{II}(x) \quad -h/2 \leq y \leq h/2 \quad (4)$$

$$H_z^{III}(x, y) = \sum_{p=-\infty}^{\infty} t_p u_p^{III}(x) e^{-ik_{p,y}^{III} (y+h/2)} \quad y \leq -h/2 \quad (5)$$

where  $k_{p,x}^I = k_{p,x}^{III} = k_0 \sin \theta + 2\pi p / d$ ,  $k_{p,y}^I = \sqrt{k_0^2 - (k_{p,x}^I)^2}$  and  $k_{p,y}^{III} = \sqrt{\epsilon_{III} k_0^2 - (k_{p,x}^{III})^2}$  are the  $x$ - and  $y$ -components of the wavevectors in regions I and III, respectively.  $k_0 = \omega / c_0$  where  $\omega$  is the frequency of the incident light and  $c_0$  is the speed of light in vacuum.  $r_p$  and  $t_p$  are the reflection and transmission coefficients at the interfaces between the regions I and II, and between the regions II and III for the diffraction order  $p$ , respectively.  $u_p^i(x)$  is the field distribution along the  $x$ -direction in the region  $i$  ( $i = I, II, III$ ). In the regions I and III, the fields are expanded in the plane wave basis, i.e.,  $u_p^I(x) = u_p^{III}(x) = e^{ik_{p,x}^I x} / \sqrt{d}$ . In the region II, the field distribution  $u^{II}(x)$  is obtained by solving the Helmholtz equation:

$$k(x)^2 \frac{\partial}{\partial x} \left( \frac{1}{k(x)^2} \frac{\partial}{\partial x} u^{II}(x) \right) + (\epsilon_m - \epsilon_d) k_0^2 \Theta(x-w) u^{II}(x) = -\beta^2 u^{II}(x) \quad (6)$$

where the wavevector  $k(x)$  and the Heaviside step function  $\Theta(x-w)$  are given as:

$$k(x) = \begin{cases} \sqrt{\epsilon_d} k_0 & 0 \leq x \leq w \\ \sqrt{\epsilon_m} k_0 & w < x \leq d \end{cases} \quad \Theta(x-w) = \begin{cases} 0 & x < w \\ 1 & x > w \end{cases} \quad (7)$$

The Helmholtz equation is a second-order partial differential equation, thus the solution can be expressed by two linearly independent functions  $\theta(x)$  and  $\psi(x)$  under the boundary conditions at  $x = 0$  and  $x = w$  as well as the periodicity of the structure. The solutions are:

$$u^{\text{II}}(x) = \theta(x) + \gamma\psi(x) \quad (8)$$

where

$$\theta(x) = \begin{cases} \cos(k_x^d x) & 0 \leq x \leq w \\ \cos(k_x^d w) \sin(k_x^m (x-w)) - \frac{k_x^d}{k_x^m} \sin(k_x^d w) \sin(k_x^m (x-w)) & w \leq x \leq d \end{cases} \quad (9)$$

$$\psi(x) = \begin{cases} \frac{1}{k_x^d} \sin(k_x^d x) & 0 \leq x \leq w \\ \frac{1}{k_x^d} \sin(k_x^d w) \cos(k_x^m (x-w)) + \frac{1}{k_x^m} \cos(k_x^d w) \sin(k_x^m (x-w)) & w \leq x \leq d \end{cases} \quad (10)$$

where  $k_x^d = \sqrt{\epsilon_d k_0^2 - \beta^2}$  and  $k_x^m = \sqrt{\epsilon_m k_0^2 - \beta^2}$  are the  $x$ -component of the wavevector in the dielectric and metal in the region II, respectively, for the anti-symmetric surface mode with the propagation constant  $\beta$ , and  $\gamma = (e^{ik_0 \sin \theta d} - \theta(d)) / \psi(d)$  is introduced due to the periodic boundary condition.

The reflection and transmission coefficients as well as the field amplitudes  $a$  and  $b$  can be uniquely determined by imposing the boundary conditions at the two interfaces  $y = h/2$  and  $y = -h/2$ . In general, the reflectance of the light is given as the sum of all of the diffraction orders. However, in the structure of our interest, only the zeroth diffracted wave (i.e., with  $p = 0$ ) is non-evanescent. Therefore, the contribution to the reflectance of the structure in the far-field solely comes from the zeroth mode of the reflection coefficient  $r_0$ . The two boundary conditions at the two interfaces  $y = h/2$  and  $y = -h/2$  give the four algebraic equations. Then, we can solve these to determine coefficient  $a$  and  $b$  in Eq. (4). Using the obtained coefficients, we can determine the reflection coefficient  $r_0$  as:

$$r_0 = 1 - 2i \frac{(\beta / k_{0,y}^I) |A_0|^2 (\coth(\beta h) + iK)}{1 - MK + i(M + K) \coth(\beta h)} \quad (11)$$

where  $M = \sum_{p=-\infty}^{\infty} (\beta / k_{p,y}^I) |A_p|^2$ ,  $K = \sum_{p=-\infty}^{\infty} (\beta / k_{p,y}^{\text{III}}) |A_p|^2$  and  $A_p$  is the field overlap integral between regions I (or III) and II:

$$A_p = \int_0^d dx \frac{1}{(k_{\text{II}}^2(x))^*} (u_p^{\text{I}}(x))^* u_p^{\text{II}}(x) \quad k_{\text{II}}(x) = \begin{cases} \sqrt{\epsilon_d} k_0 & 0 \leq x \leq w \\ \sqrt{\epsilon_m} k_0 & w \leq x \leq d \end{cases} \quad (12)$$

The propagation constant  $\beta$  can be obtained by solving the dispersion relation that, in its general form, depends on the periodicity of the structure. However, it is well approximated by the dispersion relation of the infinitely-long single metal-dielectric-metal waveguide Eq. (2), as the skin depth of the anti-symmetric mode is much smaller than the distance between two nanoslits, such that each nanoslit is effectively isolated from adjacent nanoslits. The propagation constant  $\beta$  of the anti-symmetric surface mode obtained from Eq. (2) is inserted into Eq. (11), and the reflectance of the structure for the  $p$ -polarized incident light is obtained as  $R = |r_0|^2$ . Since the magnetic field near the surface at  $y = h/2$  exhibits strong local spatial

variations, the summation up to around  $p = 30$  is necessary to achieve the convergence of the reflectance.

The spectral reflectance of the structure in Fig. 3 (b) calculated with the finite-element method (blue dots) is compared to the predictions obtained by the semi-analytical expression Eq. (11) with the propagation constants obtained by solving Eq. (2) (red line). The result is shown in Fig. 5 (a). It can be seen that the semi-analytical model predicts a slightly blue shifted peak position by about 40nm. We found that the effective refractive index of the surface mode obtained from the solution of the dispersion relation in Eq. (2) is slightly different from that obtained by the rigorous FDTD simulation. Remember that the dispersion relation Eq. (2) is strictly valid for an infinitely-long single MDM waveguide while our structure is composed of periodic truncated MDM nanoslits [58]. We calculated rigorously the effective refractive index of the surface mode supported in the periodic nanoslits by the FDTD technique. We used the same boundary conditions as mentioned for the finite-element method. In fact, the propagation constant obtained by Eq. (2) differs by the amount of  $\Delta n_{eff} \sim 0.02$  compared to the rigorous numerical result obtained by the mode expansion in FDTD simulation, which caused the shift of resonant peak. The semi-analytical expression using the propagation constant  $\beta$  calculated by the FDTD method as input is shown in the green line in Fig. 5 (a) and shows a good agreement with the numerical simulation. It is considered that the deviation in  $\beta$  is due to a shallow depth of the nanoslit, which leads to the approximation of the propagation constant by the solution of Eq. (2) less accurate. However, as the nanoslit depth becomes longer, the solution of the dispersion relation Eq. (2) is a good approximation to the actual effective refractive index. In fact, Fig. 5 (b) shows the spectral reflectance of the structure in Fig. 3 (c) and the semi-analytical expression with the solution of Eq. (2) as an input shows a good agreement with the numerical result by the finite element method. Thus, we conclude that the perfect absorption of light is indeed due to the critical coupling to the anti-symmetric surface mode, and the semi-analytical model shows a good agreement with the numerical simulation. However, one should note that the use of the propagation constant obtained by Eq. (2) to the model is invalid when the nanoslit depth is too shallow. In fact, this point is also mentioned in the modeling of extraordinary transmission through nanoslits [58].

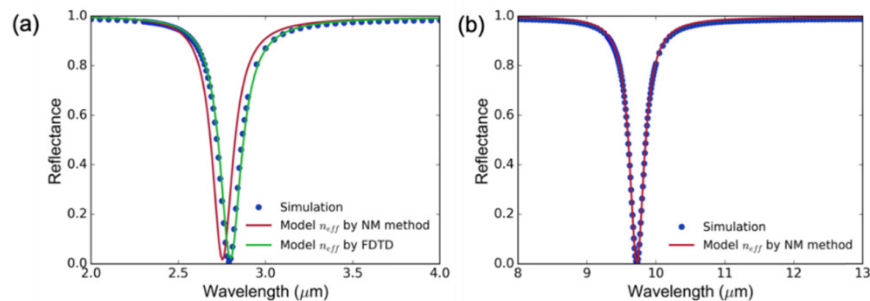


Fig. 5. Comparison of spectral reflectance between the numerical simulation (dots) and the semi-analytical results (solid lines) obtained by Eq. (11) for: (a) structure shown in Fig. 2 (b) and (b) structure shown in Fig. 2 (c). For (a), the propagation constant  $\beta$  is calculated by two methods: the solution of Eq. (2) (red line) and the rigorous mode expansion in FDTD simulation (green line) and for (b), the solution of Eq. (2) is used.

#### 4. Results and discussion

The surface mode supported in the periodic nanoslit structure can achieve the large enhancement of electric and magnetic fields in the nanoslit. As shown in Fig. 6 (a), the structure in Fig. 3 (b) can achieve more than 30 (10) times enhancement in the magnetic (electric) field magnitude inside the nanoslit when normalized by the incident magnetic (electric) field at the resonant wavelength  $\lambda = 2.79\mu\text{m}$ . This translates into over 900 (100)-fold

enhancement in the corresponding field intensities. The corresponding  $Q$  factor or the absorption resonance is estimated to be  $\sim 20$ , or equivalently  $\Gamma/\omega_0 \sim 0.05$  where  $\Gamma$  and  $\omega_0$  are the linewidth and the resonant frequency in the spectrum shown in Fig. 3 (b). The  $Q$  factors of the resonances in Fig. 3 (a) and (c) are  $\sim 24$  and  $\sim 37$ , respectively. These  $Q$  factors are slightly better than previously reported plasmonic perfect absorbers in the visible ( $Q \sim 20$ ) [60], and in the near infrared ( $Q \sim 5$ ) [25] but smaller than ultra-narrow band absorbers which reported the quality factor over 60 [61–65]. The mechanisms of the ultra-narrow bandwidth include but not limited to the use of SPPs close to the light line where the dissipative loss of SPPs becomes small [61], the coupling of diffracted wave into localized SPPs [62], the Fano resonance between two localized SPP modes supported at asymmetric metallic ellipsoids [63], and the hybrid mode of two SPPs supported by two different nanostructures [64]. The use of the anti-symmetric surface mode supported between two silver nanodisks also yielded the ultra-narrow band absorber [65].

The large enhancement in the magnetic field in the nanoslit is due to the excitation of anti-parallel current in the two metallic materials that sandwich the dielectric material of the nanoslit. This creates a virtual current loop around the nanoslit as shown by the arrows in Fig. 6 (a). A virtual current loop is known to cause a large magnetic response [66,67]. This large magnetic response can find applications based on optical magnetism including sensing [68]. The Poynting vector plot in Fig. 6 (a) (white arrows) illustrates the optical power flow pathway through the absorber and reveals how the incident light, which comes from a larger area, is strongly squeezed into the nanoslit and absorbed into the metal and substrate.

The periodic nanoslit structure designed as a perfect absorber for  $p$ -polarized light exhibits strong polarization selectivity. Figure 6 (b) shows the spectral reflectance of the structure shown in Fig. 3 (b) for  $s$ - (red line) and  $p$ - (blue line) polarized normally incident light. The spectral reflectance for the  $s$ -polarized light is close to that of the bulk silver surface since no mode is excited in the nanoslit and the areal coverage of the dielectric in Fig. 3 (b) is very low ( $w/d = 6.7\%$ ). This drastic difference between the two polarizations combined with the large field enhancement can find applications in sensing such as surface-enhanced Raman spectroscopy or phase-sensing using the spectroscopic ellipsometry [62,69,70]. Moreover, the small areal coverage of the dielectric gives the structure good thermal stability due to efficient heat dissipation through the metal and substrate.

Furthermore, the angular spectrum of reflectance can also be tailored. Although the structure is designed in such a way that supports only the single anti-symmetric surface mode inside the nanoslit, the SPPs can still be supported at the surface of the structure via the lateral momentum gain due to the periodicity. However, at longer wavelengths, noble metals are low loss reflectors. Thus, the propagation length of SPPs at the surface is long enough so that the excited surface plasmons will mostly be scattered back to the free-space rather than dissipated. Therefore, by varying the period of the structure, one can excite the SPPs at the surface for the incident light from a given angle of incidence and make the structure reflective for the light coming from this angle. This means that a good absorber at the resonant wavelength can turn into a good reflector for a given angle of incidence without affecting much the absorption spectrum for other angles. The resonant condition of the SPPs is given as  $k_{SP} = k_0 \sin \theta + 2\pi j / d$  where  $k_{SP}$  is the wavevector of the SPPs in  $x$ -direction and  $j$  is an integer. As the frequency of interest is much smaller than the plasma frequency of silver, the surface plasmons mode is close to the light line, i.e.,  $k_{SP} \sim k_0$ . Therefore, the resonant condition of the SPPs excitation is approximated as  $\sin \theta \approx 1 - j\lambda / d$ . We see from this equation that the structure in Fig. 3 (a) does not have a real-valued solution. Therefore, the SPPs at the surface are not supported in the structure Fig. 3 (a). Combined with the fact that the nanoslit width is much smaller than the wavelength, the nanoslit functions as an isotropic absorber at the resonant wavelength as shown

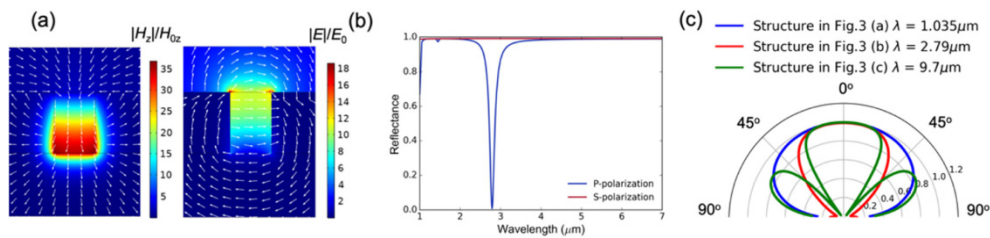


Fig. 6. Applications of periodic nanoslit structures (a) Electric and magnetic field enhancement (heat maps) at the resonant wavelength of the structure in Fig. 3 (b). The distribution of the Poynting vector is shown as white arrows in the magnetic field plot on the left. The electric current density vector is shown as white arrows in the electric field plot on the right. The vectors are normalized and thus the length of the vectors indicates only the direction, but not the magnitude. (b) Polarization selectivity of spectral reflectance for normal incident light; (c) Angular spectrum of the absorptance (emittance) of the three structures in Fig. 3 at the corresponding resonant frequencies.

in Fig. 6 (c). For the structure in Fig. 3 (b) and (c), the SPPs can be excited at the incident angles  $\theta = 83^\circ$  and  $\theta = 38^\circ$ , respectively which agrees well with the shunt in absorptance in the angular distributions shown in Fig. 6 (c). Thus, by varying the period, one can design either a directional absorber or an isotropic absorber.

This ability to independently tailor the spectral and angular reflectance is due to the orthogonality of the propagation directions of the SPPs in the nanoslit and on top of the structure. Owing to the reciprocity between the absorptance and emittance of a surface at a given frequency and angle in thermal equilibrium (i.e., Kirchhoff's law), periodic nanoslit structures can find applications as partially-coherent thermal emitters [8,71–74]. The angular emittance of the structure in Fig. 3 (b) shows directionality in the normal direction. This could be especially useful for applications such as thermophotovoltaics (TPV) where a high emittance to large angles leads to radiative losses due to small view factor [75–80]. Moreover, it is known that the absorption cross section becomes large for directional absorbers [43,81]. This is considered to be the reason why the design in Fig. 3 (b) can attain the complete absorption for the period that is 20 times greater than the nanoslit width. Finally, the structure shows high reflectance for longer wavelengths than the resonant wavelength since we excite the anti-symmetric surface mode at the lowest order of the Fabry-Perot resonance. This is especially important for engineering thermal emitters for TPV and partially-coherent thermal infrared sources as the structure does not exhibit emission at longer wavelengths, which would otherwise result in the efficiency loss and contamination of the thermal emission spectrum.

The strong confinement of the anti-symmetric surface mode results in the complete absorption of light that is incident from more than 10 times greater area than the nanoslit width, and the spatial confinement in the lateral direction makes each nanoslit independent of each other. This fact allows us to create the structure that attains complete absorption of light at multiple wavelengths by inserting two (or more) nanoslits supporting different resonant wavelengths within one period of the structure. Figure 7 (a) shows the same nanoslit structure as in Fig. 1 except two nanoslits are located in one period. The nanoslits are designed so that they support resonant frequencies at around  $2.4 \mu\text{m}$  and  $4 \mu\text{m}$ , respectively. The spectral reflectance of the *p*-polarized normally incident light is shown in Fig. 7 (b). As shown, the structure achieves the complete absorption of light at around the two chosen wavelengths. The magnetic field distributions normalized by the incident magnetic field in the structure at the two wavelengths are shown in Fig. 7 (c). It is observed that the magnetic field is selectively enhanced at the two nanoslits at the two resonant wavelengths, respectively. As each nanoslit is independent of each other, one can create multi-band absorbers as far as each nanoslit is capable of absorbing all the incident light in one period. Thus, the structure can find applications in spatial and spectral light separation [47]. Our simulation shows that two

spectra that are separated by more than  $1\mu\text{m}$  in wavelength can also be sorted by designing the structure appropriately.

In actual fabrication, the edges at the top and bottom of the nanoslit structure would have fillets depending on the resolution of fabrication methods and the material properties. We also investigated the effects of fillets on spectral absorptance. Figure 8 shows the spectral absorptance of the periodic nanoslit structure with the same geometrical parameters as those in Fig. 3 (b) but with fillets of the radius  $w/3$  at the four edges of the nanoslit as shown in the inset of Fig. 8. The structure shows the complete absorption of light even in the presence of the fillets. The resonant wavelength is blue shifted, likely due to an effectively wider nanoslit width as we discussed in Fig. 4 (b). The  $Q$ -factor of the resonance is found to be  $\sim 20$ , which did not change from that without the fillets. Therefore, the existence of fillets does not degrade either the spectral absorptance or the  $Q$  factor, which demonstrates the robustness of the structure for actual applications.

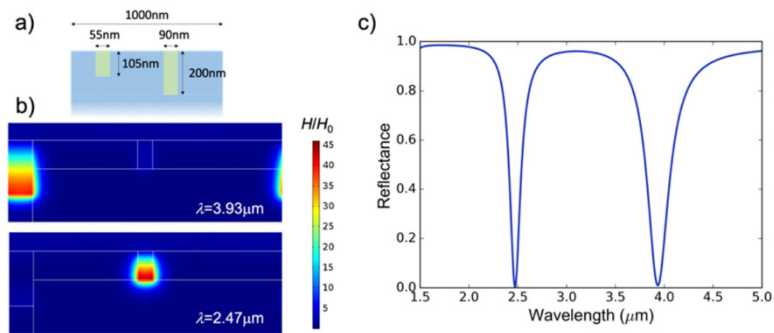


Fig. 7. Complete absorption of light at two different wavelengths supported by two nanoslits. (a) A schematic of the two-nanoslit structure. (b) The spatial distribution of magnetic field normalized by the incident magnetic field at the two resonant wavelengths. (c) The corresponding dual-band reflectance spectrum. For the dielectric constant of silicon, we used  $\epsilon_{Si} = 11.79$ .

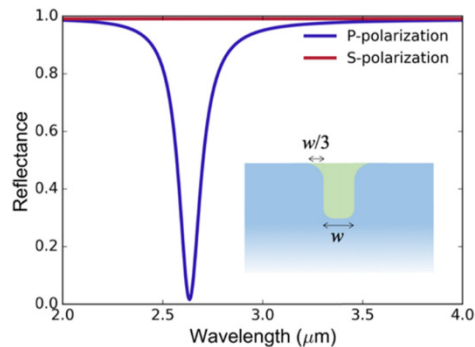


Fig. 8. Spectral reflectance of periodic nanoslit structure for normally incident  $p$ -polarized light with realistic fillets at the edges of the nanoslit. The geometrical parameter, as well as materials, are the same as those in the structure in Fig. 3 (b). The radius of the fillets is  $w/3$ .

## 5. Conclusions

In conclusion, we investigated the optical absorption of the periodic nanoslit structure supporting the single electric-field anti-symmetric surface mode. We demonstrated that perfect absorption of  $p$ -polarized light can be achieved at different wavelengths from the visible to the mid-infrared just by varying geometrical parameters. The perfect absorption of light into the nanoslits with the width more than 10 times smaller than the period is revealed to emerge due to the creation of virtual current loop around the nanoslit, which enhances the

magnetic response of the structure drastically. We studied the different roles played by the periodicity, width, and the depth of the nanoslit in manipulating the spectral characteristics of the absorber. The resonant frequency is mainly determined by the nanoslit depth due to the excitation of the Fabry-Perot resonance in the vertical direction, while the nanoslit width and the structure period can be tuned to achieve the perfect absorption at the chosen resonant frequency. We showed that the SPPs at the surface is not responsible for the absorption, and thus can be used for tailoring the angular distribution of reflectance, or – by reciprocity – of thermal emittance. We developed the semi-analytical model that provides the physical explanation of the perfect absorption and can also be used for the fast implementation of the structure forward and inverse design and optimization. The periodic nanoslit structure can be a platform for optical sensing and polarization control due to its clear contrast of spectral reflectance between the two polarizations and strong field enhancement. Moreover, the structure can be designed as a multi-band perfect absorber for *p*-polarized light, which realizes optical sensing of multiple components in one platform and allows for the spatial and spectral light sorting into nano-scale areas. Finally, a large areal coverage of flat metal surfaces, as well as the tunability of the angular reflectance, make the structure a good directional thermal emitter with suppressed long-wavelength parasitic emittance, which shows promise for thermophotovoltaics and thermal infrared sources development.

## Funding

DOE BES (DE-FG02-02ER45977).

## References

1. M. Li, S. K. Cushing, and N. Wu, "Plasmon-enhanced optical sensors: a review," *Analyst (Lond.)* **140**(2), 386–406 (2015).
2. S. Lal, S. Link, and N. J. Halas, "Nano-optics from sensing to waveguiding," *Nat. Photonics* **1**(11), 641–648 (2007).
3. M. L. Brongersma, Y. Cui, and S. Fan, "Light management for photovoltaics using high-index nanostructures," *Nat. Mater.* **13**(5), 451–460 (2014).
4. H. A. Atwater and A. Polman, "Plasmonics for improved photovoltaic devices," *Nat. Mater.* **9**(3), 205–213 (2010).
5. A. Sobhani, M. W. Knight, Y. Wang, B. Zheng, N. S. King, L. V. Brown, Z. Fang, P. Nordlander, and N. J. Halas, "Narrowband photodetection in the near-infrared with a plasmon-induced hot electron device," *Nat. Commun.* **4**(1), 1643 (2013).
6. D. Costantini, A. Lefebvre, A.-L. Coutrot, I. Moldovan-Doyen, J.-P. Hugonin, S. Boutami, F. Marquier, H. Benisty, and J.-J. Greffet, "Plasmonic Metasurface for Directional and Frequency-Selective Thermal Emission," *Phys. Rev. Appl.* **4**(1), 014023 (2015).
7. M. Laroche, C. Arnold, F. Marquier, R. Carminati, J.-J. Greffet, S. Collin, N. Bardou, and J.-L. Pelouard, "Highly directional radiation generated by a tungsten thermal source," *Opt. Lett.* **30**(19), 2623–2625 (2005).
8. E. Hasman, V. Kleiner, N. Dahan, Y. Gorodetski, K. Frischwasser, and I. Balin, "Manipulation of thermal emission by use of micro and nanoscale structures," *J. Heat Transfer* **134**(3), 031023 (2012).
9. D. M. Bierman, A. Lenert, W. R. Chan, B. Bhatia, I. Celanović, M. Soljačić, and E. N. Wang, "Enhanced photovoltaic energy conversion using thermally based spectral shaping," *Nat. Energy* **1**(6), 16068 (2016).
10. P. Bermel, S. V. Boriskina, Z. Yu, and K. Joulain, "Control of radiative processes for energy conversion and harvesting," *Opt. Express* **23**(24), A1533–A1540 (2015).
11. T. W. Ebbesen, H. J. Lezec, H. F. Ghaemi, T. Thio, and P. A. Wolff, "Extraordinary optical transmission through sub-wavelength hole arrays," *Nature* **391**(6668), 667–669 (1998).
12. L. Martin-Moreno, F. J. García-Vidal, H. J. Lezec, K. M. Pellerin, T. Thio, J. B. Pendry, and T. W. Ebbesen, "Theory of Extraordinary Optical Transmission through Subwavelength Hole Arrays," *Phys. Rev. Lett.* **86**(6), 1114–1117 (2001).
13. T. V. Teperik, V. V. Popov, and F. J. García de Abajo, "Void plasmons and total absorption of light in nanoporous metallic films," *Phys. Rev. B Condens. Matter Mater. Phys.* **71**(8), 085408 (2005).
14. V. G. Kravets, F. Schedin, and A. N. Grigorenko, "Plasmonic blackbody: Almost complete absorption of light in nanostructured metallic coatings," *Phys. Rev. B Condens. Matter Mater. Phys.* **78**(20), 205405 (2008).
15. Y. Huang, C. Min, and G. Veronis, "Compact slit-based couplers for metal-dielectric-metal plasmonic waveguides," *Opt. Express* **20**(20), 22233–22244 (2012).
16. R.-L. Chern, Y.-T. Chen, and H.-Y. Lin, "Anomalous optical absorption in metallic gratings with subwavelength slits," *Opt. Express* **18**(19), 19510–19521 (2010).
17. C. Min, L. Yang, and G. Veronis, "Microcavity enhanced optical absorption in subwavelength slits," *Opt.*

- Express **19**(27), 26850–26858 (2011).
18. I. S. Spevak, A. Y. Nikitin, E. V. Bezuglyi, A. Levchenko, and A. V. Kats, “Resonantly suppressed transmission and anomalously enhanced light absorption in periodically modulated ultrathin metal films,” *Phys. Rev. B Condens. Matter Mater. Phys.* **79**(16), 161406 (2009).
  19. M. C. Hutley and D. Maystre, “The total absorption of light by a diffraction grating,” *Opt. Commun.* **19**(3), 431–436 (1976).
  20. E. Popov, D. Maystre, R. C. McPhedran, M. Nevière, M. C. Hutley, and G. H. Derrick, “Total absorption of unpolarized light by crossed gratings,” *Opt. Express* **16**(9), 6146–6155 (2008).
  21. N. I. Landy, S. Sajuyigbe, J. J. Mock, D. R. Smith, and W. J. Padilla, “Perfect Metamaterial Absorber,” *Phys. Rev. Lett.* **100**(20), 207402 (2008).
  22. C. M. Watts, X. Liu, and W. J. Padilla, “Metamaterial Electromagnetic Wave Absorbers,” *Adv. Mater.* **24**(23), OP181 (2012).
  23. K. Kneipp, H. Kneipp, I. Itzkan, R. R. Dasari, and M. S. Feld, “Surface-enhanced Raman scattering and biophysics,” *J. Phys. Condens. Matter* **14**(18), 202 (2002).
  24. K. Kneipp, Y. Wang, H. Kneipp, L. T. Perelman, I. Itzkan, R. R. Dasari, and M. S. Feld, “Single Molecule Detection Using Surface-Enhanced Raman Scattering (SERS),” *Phys. Rev. Lett.* **78**(9), 1667–1670 (1997).
  25. N. Liu, M. Mesch, T. Weiss, M. Hentschel, and H. Giessen, “Infrared Perfect Absorber and Its Application As Plasmonic Sensor,” *Nano Lett.* **10**(7), 2342–2348 (2010).
  26. M. C. Beard, J. M. Luther, and A. J. Nozik, “The promise and challenge of nanostructured solar cells,” *Nat. Nanotechnol.* **9**(12), 951–954 (2014).
  27. L. Tsakalakos, “Nanostructures for photovoltaics,” *Mater. Sci. Eng. Rep.* **62**(6), 175–189 (2008).
  28. W. L. Barnes, A. Dereux, and T. W. Ebbesen, “Surface plasmon subwavelength optics,” *Nature* **424**(6950), 824–830 (2003).
  29. E. Betzig and J. K. Trautman, “Near-field optics: microscopy, spectroscopy, and surface modification beyond the diffraction limit,” *Science* **257**(5067), 189–195 (1992).
  30. M. Kreiter, J. Oster, R. Sambles, S. Herminghaus, S. Mittler-Neher, and W. Knoll, “Thermally induced emission of light from a metallic diffraction grating, mediated by surface plasmons,” *Opt. Commun.* **168**(1–4), 117–122 (1999).
  31. M.-W. Tsai, T.-H. Chuang, C.-Y. Meng, Y.-T. Chang, and S.-C. Lee, “High performance midinfrared narrow-band plasmonic thermal emitter,” *Appl. Phys. Lett.* **89**(17), 173116 (2006).
  32. H. Sai, Y. Kanamori, and H. Yugami, “Tuning of the thermal radiation spectrum in the near-infrared region by metallic surface microstructures,” *J. Micromech. Microeng.* **15**(9), S243–S249 (2005).
  33. J.-J. Greffet, R. Carminati, K. Joulain, J.-P. Mulet, S. Mainguy, and Y. Chen, “Coherent emission of light by thermal sources,” *Nature* **416**(6876), 61–64 (2002).
  34. R. W. Wood, “Anomalous Diffraction Gratings,” *Phys. Rev.* **48**(12), 928–936 (1935).
  35. A. Hessel and A. A. Oliner, “A New Theory of Wood’s Anomalies on Optical Gratings,” *Appl. Opt.* **4**(10), 1275 (1965).
  36. F. Marquier, K. Joulain, J. P. Mulet, R. Carminati, and J. J. Greffet, “Engineering infrared emission properties of silicon in the near field and the far field,” *Opt. Commun.* **237**(4–6), 379–388 (2004).
  37. J. A. Schuller, E. S. Barnard, W. Cai, Y. C. Jun, J. S. White, and M. L. Brongersma, “Plasmonics for extreme light concentration and manipulation,” *Nat. Mater.* **9**(3), 193–204 (2010).
  38. A. Gopinath, S. V. Boriskina, B. M. Reinhard, and L. Dal Negro, “Deterministic aperiodic arrays of metal nanoparticles for surface-enhanced Raman scattering (SERS),” *Opt. Express* **17**(5), 3741–3753 (2009).
  39. M. G. Nielsen, D. K. Gramotnev, A. Pors, O. Albrektsen, and S. I. Bozhevolnyi, “Continuous layer gap plasmon resonators,” *Opt. Express* **19**(20), 19310–19322 (2011).
  40. M. G. Nielsen, A. Pors, O. Albrektsen, and S. I. Bozhevolnyi, “Efficient absorption of visible radiation by gap plasmon resonators,” *Opt. Express* **20**(12), 13311–13319 (2012).
  41. K. Aydin, V. E. Ferry, R. M. Briggs, and H. A. Atwater, “Broadband polarization-independent resonant light absorption using ultrathin plasmonic super absorbers,” *Nat. Commun.* **2**(1), 517 (2011).
  42. J. S. White, G. Veronis, Z. Yu, E. S. Barnard, A. Chandran, S. Fan, and M. L. Brongersma, “Extraordinary optical absorption through subwavelength slits,” *Opt. Lett.* **34**(5), 686–688 (2009).
  43. L. Verslegers, Z. Yu, P. B. Catrysse, and S. Fan, “Temporal coupled-mode theory for resonant apertures,” *J. Opt. Soc. Am. B* **27**(10), 1947 (2010).
  44. P. Berini, “Long-range surface plasmon polaritons,” *Adv. Opt. Photonics* **1**(3), 484 (2009).
  45. H. T. Miyazaki and Y. Kurokawa, “Squeezing Visible Light Waves into a 3-nm-Thick and 55-nm-Long Plasmon Cavity,” *Phys. Rev. Lett.* **96**(9), 097401 (2006).
  46. T. Tamir, ed., *Guided-Wave Optoelectronics*, Springer Series in Electronics and Photonics (Springer Berlin Heidelberg, 1988), **26**.
  47. S. J. Kim, J.-H. Kang, M. Mutlu, J. Park, W. Park, K. E. Goodson, R. Sinclair, S. Fan, P. G. Kik, and M. L. Brongersma, “Anti-Hermitian photodetector facilitating efficient subwavelength photon sorting,” *Nat. Commun.* **9**(1), 316 (2018).
  48. B. Prade, J. Y. Vinet, and A. Mysyrowicz, “Guided optical waves in planar heterostructures with negative dielectric constant,” *Phys. Rev. B Condens. Matter* **44**(24), 13556–13572 (1991).
  49. D.-K. Qing and G. Chen, “Nanoscale optical waveguides with negative dielectric claddings,” *Phys. Rev. B Condens. Matter Mater. Phys.* **71**(15), 153107 (2005).

50. E. D. Palik, *Handbook of Optical Constants of Solids* (Academic Press, 1985).
51. H. U. Yang, J. D'Archangel, M. L. Sundheimer, E. Tucker, G. D. Boreman, and M. B. Raschke, "Optical dielectric function of silver," *Phys. Rev. B Condens. Matter Mater. Phys.* **91**(23), 235137 (2015).
52. J. A. Dionne, L. A. Sweatlock, H. A. Atwater, and A. Polman, "Plasmon slot waveguides: Towards chip-scale propagation with subwavelength-scale localization," *Phys. Rev. B Condens. Matter Mater. Phys.* **73**(3), 035407 (2006).
53. J. A. Nelder and R. Mead, "A Simplex Method for Function Minimization," *Comput. J.* **7**(4), 308–313 (1965).
54. R. Gordon, "Light in a subwavelength slit in a metal: Propagation and reflection," *Phys. Rev. B Condens. Matter Mater. Phys.* **73**(15), 153405 (2006).
55. L. C. Botten, M. S. Craig, and R. C. McPhedran, "Highly Conducting Lamellar Diffraction Gratings," *Opt. Acta (Lond.)* **28**(8), 1103–1106 (1981).
56. L. C. Botten, M. S. Craig, R. C. McPhedran, J. L. Adams, and J. R. Andrewartha, "The Finitely Conducting Lamellar Diffraction Grating," *Opt. Acta (Lond.)* **28**(8), 1087–1102 (1981).
57. I. C. Botten, M. S. Craig, R. C. McPhedran, J. L. Adams, and J. R. Andrewartha, "The Dielectric Lamellar Diffraction Grating," *Opt. Acta (Lond.)* **28**(3), 413–428 (1981).
58. P. Lalanne, J. P. Hugonin, S. Astilean, M. Palamaru, and K. D. Möller, "One-mode model and Airy-like formulae for one-dimensional metallic gratings," *J. Opt. A, Pure Appl. Opt.* **2**(1), 48–51 (2000).
59. J. Le Perchec, P. Quémerais, A. Barbara, and T. López-Ríos, "Why Metallic Surfaces with Grooves a Few Nanometers Deep and Wide May Strongly Absorb Visible Light," *Phys. Rev. Lett.* **100**(6), 066408 (2008).
60. J. Hao, L. Zhou, and M. Qiu, "Nearly total absorption of light and heat generation by plasmonic metamaterials," *Phys. Rev. B Condens. Matter Mater. Phys.* **83**(16), 165107 (2011).
61. L. Meng, D. Zhao, Z. Ruan, Q. Li, Y. Yang, and M. Qiu, "Optimized grating as an ultra-narrow band absorber or plasmonic sensor," *Opt. Lett.* **39**(5), 1137–1140 (2014).
62. V. G. Kravets, F. Schedin, R. Jalil, L. Britnell, R. V. Gorbachev, D. Ansell, B. Thackray, K. S. Novoselov, A. K. Geim, A. V. Kabashin, and A. N. Grigorenko, "Singular phase nano-optics in plasmonic metamaterials for label-free single-molecule detection," (2013).
63. M. Zhang, J. Fang, F. Zhang, J. Chen, and H. Yu, "Ultra-narrow band perfect absorbers based on Fano resonance in MIM metamaterials," *Opt. Commun.* **405**, 216–221 (2017).
64. Z. Li, S. Butun, and K. Aydin, "Ultrathin Band Absorbers Based on Surface Lattice Resonances in Nanostructured Metal Surfaces," *ACS Nano* **8**(8), 8242–8248 (2014).
65. Z. Yong, S. Zhang, C. Gong, and S. He, "Narrow band perfect absorber for maximum localized magnetic and electric field enhancement and sensing applications," *Sci. Rep.* **6**(1), 24063 (2016).
66. A. K. Sarychev, G. Shvets, and V. M. Shalaev, "Magnetic plasmon resonance," *Phys. Rev. E Stat. Nonlin. Soft Matter Phys.* **73**(3), 036609 (2006).
67. M. Lorente-Crespo, L. Wang, R. Ortuño, C. García-Meca, Y. Ekinici, and A. Martínez, "Magnetic Hot Spots in Closely Spaced Thick Gold Nanorings," *Nano Lett.* **13**(6), 2654–2661 (2013).
68. P. C. Wu, G. Sun, W. T. Chen, K.-Y. Yang, Y.-W. Huang, Y.-H. Chen, H. L. Huang, W.-L. Hsu, H. P. Chiang, and D. P. Tsai, "Vertical split-ring resonator based nanoplasmonic sensor," *Appl. Phys. Lett.* **105**(3), 033105 (2014).
69. Y. Tsurimaki, J. K. Tong, V. N. Boriskina, A. Semenov, M. I. Ayzatsky, Y. P. Machekhin, G. Chen, and S. V. Boriskina, "Topological Engineering of Interfacial Optical Tamm States for Highly Sensitive Near-Singular-Phase Optical Detection," *ACS Photonics* **5**(3), 929–938 (2018).
70. S. V. Boriskina and Y. Tsurimaki, "Sensitive singular-phase optical detection without phase measurements with Tamm plasmons," *J. Phys. Condens. Matter* **30**(22), 224003 (2018).
71. S. V. Boriskina, J. K. Tong, W.-C. Hsu, B. Liao, Y. Huang, V. Chiloyan, and G. Chen, "Heat meets light on the nanoscale," *Nanophotonics* **5**(1), 134–160 (2016).
72. S. V. Boriskina, T. A. Cooper, L. Zeng, G. Ni, J. K. Tong, Y. Tsurimaki, Y. Huang, L. Meroueh, G. Mahan, and G. Chen, "Losses in plasmonics: from mitigating energy dissipation to embracing loss-enabled functionalities," *Adv. Opt. Photonics* **9**(4), 775 (2017).
73. M. I. Stockman, K. Kneipp, S. I. Bozhevolnyi, S. Saha, A. Dutta, J. Ndukaife, N. Kinsey, H. Reddy, U. Guler, V. M. Shalaev, A. Boltasseva, B. Gholipour, H. N. S. Krishnamoorthy, K. F. MacDonald, C. Soci, N. I. Zheludev, V. Savinov, R. Singh, P. Groß, C. Lienau, M. Vadai, M. L. Solomon, D. R. Barton III, M. Lawrence, J. A. Dionne, S. V. Boriskina, R. Esteban, J. Aizpurua, X. Zhang, S. Yang, D. Wang, W. Wang, T. W. Odom, N. Accanto, P. M. de Roque, I. M. Hancu, L. Piatkowski, N. F. van Hulst, and M. F. Kling, "Roadmap on plasmonics," *J. Opt.* **20**(4), 043001 (2018).
74. J.-J. Greffet, R. Carminati, K. Joulain, J.-P. Mulet, S. Mainguy, and Y. Chen, "Coherent emission of light by thermal sources," *Nature* **416**(6876), 61–64 (2002).
75. S. Molesky, C. J. Dewalt, and Z. Jacob, "High temperature epsilon-near-zero and epsilon-near-pole metamaterial emitters for thermophotovoltaics," *Opt. Express* **21**(S1), A96–A110 (2013).
76. T. J. Coutts, "A review of progress in thermophotovoltaic generation of electricity," *Renew. Sustain. Energy Rev.* **3**(2–3), 77–184 (1999).
77. J. K. Tong, W.-C. Hsu, Y. Huang, S. V. Boriskina, and G. Chen, "Thin-film "Thermal Well" emitters and absorbers for high-efficiency thermophotovoltaics," *Sci. Rep.* **5**(1), 10661 (2015).
78. P. Bermel, M. Ghebrebrhan, W. Chan, Y. X. Yeng, M. Araghchini, R. Hamam, C. H. Marton, K. F. Jensen, M. Soljačić, J. D. Joannopoulos, S. G. Johnson, and I. Celanovic, "Design and global optimization of high-

- efficiency thermophotovoltaic systems,” *Opt. Express* **18**(S3 Suppl 3), A314–A334 (2010).
79. Y. Nam, Y. X. Yeng, A. Lenert, P. Bermel, I. Celanovic, M. Soljačić, and E. N. Wang, “Solar thermophotovoltaic energy conversion systems with two-dimensional tantalum photonic crystal absorbers and emitters,” *Sol. Energy Mater. Sol. Cells* **122**, 287–296 (2014).
  80. S. V. Boriskina, M. A. Green, K. Catchpole, E. Yablonovitch, M. C. Beard, Y. Okada, S. Lany, T. Gershon, A. Zakutayev, M. H. Tahersima, V. J. Sorger, M. J. Naughton, K. Kempa, M. Dagenais, Y. Yao, L. Xu, X. Sheng, N. D. Bronstein, J. A. Rogers, A. P. Alivisatos, R. G. Nuzzo, J. M. Gordon, D. M. Wu, M. D. Wisser, A. Salleo, J. Dionne, P. Bermel, J.-J. Greffet, I. Celanovic, M. Soljagic, A. Manor, C. Rotschild, A. Raman, L. Zhu, S. Fan, and G. Chen, “Roadmap on optical energy conversion,” *J. Opt.* **18**(7), 073004 (2016).
  81. F. J. García-Vidal, H. J. Lezec, T. W. Ebbesen, and L. Martín-Moreno, “Multiple Paths to Enhance Optical Transmission through a Single Subwavelength Slit,” *Phys. Rev. Lett.* **90**(21), 213901 (2003).